One-pot Synthesis of Cellulose/MoS$_2$ Composite for Efficient Visible-light Photocatalytic Reduction of Cr(VI)

Chunxiang Lin,[a,b] Yushi Liu,[a] Qiaoquan Su,[a] Yifan Liu,[a] Yuancai Lv,[a] and Minghua Liu [a,]*

An effective cellulose/MoS$_2$ (Ce/MoS$_2$) composite was synthesized *via* a one-pot microwave-assisted ionic liquid method for the photocatalytic reduction of toxic Cr(VI). Effects of ionic liquids (ILs) on the MoS$_2$ nanostructure were considered, and the obtained composite was characterized by x-ray diffraction (XRD), scanning electron microscopy (SEM), high-resolution transmission electron microscopy (HRTEM), X-ray photoelectron spectrometry (XPS), and electrochemical impedance spectroscopy (EIS). The results indicated that the MoS$_2$ nanoplates were anchored and dispersed on the surface of the cellulose. Compared with the pristine MoS$_2$, the support of the cellulose greatly enhanced the photocatalytic reduction efficiency of Cr(VI) ions in solution, from 65.9% to nearly 100%. The reduction mechanism was considered, and the results implied that the simultaneous reduction of Cr(VI) during the initial dark adsorption process was observed due to the effect of citric acid as a hole scavenger. Finally, regeneration tests revealed that the Ce/MoS$_2$ composite could be recycled and reused.

Keywords: Cellulose; MoS$_2$; One-pot; Photocatalytic reduction; Cr(VI)

Contact information: a: College of Environment & Resources, Fuzhou University, 350108, Fuzhou, China;
b: Shishi Xinggang Plastic Packaging Co., Ltd., 362700, Fuzhou, China;
** Corresponding author: mhliu2000@fzu.edu.cn*

INTRODUCTION

The improper discharge of metal ions into aquatic bodies causes pollution. Hexavalent chromium (Cr(VI)), known as a carcinogen and mutagen, is an issue of concern due to its highly toxic, potentially mutagenic, and carcinogenic nature (Zhang *et al.* 2012; Ge and Ma 2015; Periyasamy *et al.* 2017). It is mobile in nature and difficult to remove from water by some common physical or chemical methods. However, another oxidation state of chromium, Cr(III), is much less toxic and carcinogenic than Cr(VI), and also much less soluble in water, so it can be easily removed in an alkaline medium (Chebeir and Liu 2016). Therefore, redox treatment is an effective and easy way to remove Cr(VI) from solution, including chemical reduction, biosorption coupled reduction, microreduction, photocatalysis, *etc*. (López-García *et al.* 2010; Bertoni *et al.* 2014; Kafilzadeh *et al.* 2016; Wang *et al.* 2016; Jiang *et al.* 2018). Chemical reduction is a traditional procedure that produces large quantities of solid sludge containing toxic chromium compounds with high cost of disposal (Remoundaki *et al.* 2010). Biomaterials and microorganisms are promising techniques for the adsorption and reduction of Cr(VI) pollution due to their low cost, environmentally-friendly character, and absence of secondary pollution. However, the efficiency to remove high concentration levels of Cr(VI) is often limited by the slow reduction kinetics (Hasin *et al.* 2010); notably, the reduction of Cr(VI) by biomaterials only has been found to occur only under strongly acidic conditions (Park *et al*. 2008). Compared with the above technologies, photocatalytic reduction of Cr(VI) to Cr(III) using photocatalysts is more effective and faster due to the remarkable chemical and photochemical stability of a semiconductor (Liu *et al.* 2011). It is a popular and promising technology for Cr(VI) removal (Bora and Mewada 2017; Christoforidis and Fornasiero 2017; Nahar *et al.* 2017; Szczepanik 2017) on account of its economical, simple, and efficient nature. The photoreduction process is often accompanied by simultaneous oxidation of organic matter in solution, which plays the role of ligand and/or sacrificial electron donor (CIESLA *et al.* 2004). Therefore, this method is especially suitable for the treatment of organic wastewater containing chromium (Mitra *et al.* 2013; Qu *et al.* 2017; Zhang *et al.* 2018). Various photocatalysts such as TiO_2, Bi-based catalyst, CdS, ZnS, and MoS_2 have been synthesized and used for photocatalytic Cr(VI) reduction and other organic pollutants degradation (Hu *et al.* 2017; Li *et al.* 2018; Soto *et al.* 2018; Wang *et al.* 2018; Yin *et al.* 2018; Shindume *et al.* 2019; Sun *et al.* 2019).

Recently, much attention has been paid to MoS_2 photocatalyst, owing to its excellent properties such as a narrow band gap (1.75 eV), large surface area, and unique morphology (Zhang *et al.* 2016). It has a special sandwich structure of three stacked atomic layers (S-Mo-S) held together by covalent bonding and an interlayer link through weak van der Waals forces (Ai *et al.* 2016). The special properties and strong absorption in the visible region of the solar spectrum make it a potential candidate as a visible-light-driven photocatalyst for water treatment.

However, some problems limit the application of MoS_2, including easy aggregation of nanoparticles and difficulty in the recovery process. To solve these problems, MoS_2 nanoparticles are often immobilized onto a support (Zhao *et al.* 2015; Li *et al.* 2016). Biomass including cellulose has been used as a support for the photocatalyst because of its excellent properties, such as biodegradability, accessibility, bio-compatibility, and high mechanical properties (Jonoobi *et al.* 2015). There are many reports about immobilization of semiconductor nanoparticles on a cellulose support with enhanced photocatalytic properties. For example, BiOBr/regenerated cellulose composites have been successfully synthesized *in situ*, and the composites show excellent photocatalytic activity for degradation of Rhodamine B (Du *et al.* 2018). Nanocellulose was used as a host for the synthesis of zinc oxide (ZnO) nanostructures through *in situ* solution casting method (Lefatshe *et al.* 2017). Mohamed *et al.* (2016) developed a regenerated cellulose/N-doped TiO_2 membrane *via* phase inversion method. However, the synthesis of cellulose-based photocatalyst materials often requires complicated, time-consuming, harsh conditions or multiple-step processes (Yang *et al.* 2016; Zhou *et al.* 2016; Wang and Mi 2017). In this regard, mild reaction conditions, time-effectiveness, and methods with low energy consumption are highly desirable.

The microwave-assisted ionic-liquid method (MAIL) has received significant attention worldwide owing to its combination of the benefits of microwave heating and ionic liquids. It is a powerful tool for the synthesis of the nanostructured materials due to the advantageous properties of rapidity and reduced energy consumption. Much progress on the preparation of nanomaterials by using this rapid method has been published, such as metal oxides (Schütz *et al.* 2017), metal sulfides (Ma *et al.* 2014), metal selenides (Tyrrell *et al.* 2015), metal tellurides (Schaumann *et al.* 2017), *etc.* A previous study revealed that ionic liquids have obvious effects on both the crystal structure and morphology of the nanomaterials (Lin *et al.* 2017).

Herein, the MAIL method was used to prepare the cellulose and immobilize MoS_2

nanoparticles with lower temperature and shorter time under ambient pressure, after which the effects of ionic liquid types on the shapes of MoS_2 were investigated. The obtained cellulose/MoS_2 composite was characterized and then applied to the reduction of Cr(VI) to Cr(III) in aqueous solution. Moreover, the reduction mechanism of Cr(VI) *via* Ce/MoS_2 composite was considered, and the stability of the composite was also evaluated.

EXPERIMENTAL

Materials and Reagents

Cotton linter was used as the cellulose material (Ce). A series of 1-butyl-3-methylimidazolium salts [BMIM]X ionic liquids (X = Cl, PF_4, BF_4, HSO_4; purity = 99%; named IL(1)–IL(4), representative [BMIM]Cl, [BMIM]PF_6, [BMIM]BF_4, [BMIM]HSO_4, respectively) were used in the experiments. Among these ILs, IL(2) through IL(4) were purchased from Shanghai Chengjie Chemical Co., Ltd (Shanghai, China), and IL(1) was obtained from Henan Lihua Pharmaceutical Co., Ltd (Henan, China). Ammonium paramolybdate ($(NH_4)_6Mo_7O_2$, ≥ 99.5%) and diphenylcarbazide were supplied by Aladdin Reagent Co., Ltd. (Shanghai, China). All other reagents were of analytical grade and utilized as received without further purification.

One-pot Synthesis of Ce/MoS_2 Composite

First, 1 g of MoS_2 precursor ($m((NH_4)_6Mo_7O_{24}):m(CH_4N_2S) = 0.6:1$) was added to 50 mL of deionized water to form transparent and uniform solution and then added to the Ce/IL mixture (in a 0.5:20 Ce–IL ratio, m/m). The mixture was stirred and sealed in a microwave reactor at 180 °C for 60 min. The resulting products were collected by centrifuging, washing repeatedly with distilled water and alcohol, and drying in a vacuum oven under 60 °C for 24 h.

To study the effects of ILs on MoS_2 structure performance, the pristine MoS_2 material was prepared by a similar procedure without the addition of cellulose. The corresponding products were labeled from MoS_2-IL1 to MoS_2-IL4, respectively. Also, pure cellulose products (Ce) were prepared by microwave-assisted ionic liquid method without adding MoS_2 precursor solution.

Materials Characterization

The crystal structures of MoS_2 and Ce/MoS_2 composites were determined with a Min Flex 600 (Rigaku, Tokyo, Japan) X-ray diffractometer (XRD). The morphologies and microstructures of the samples were investigated by field-emission scanning electron microscopy (SEM, Nova NanoSEM 230) equipped with an energy-dispersive X-ray spectroscopy (EDX) system. Transmission electron microscopy (TEM) measurements were obtained using a Tecnai G2-F20 microscope (Ames Laboratory, Ames, IA, USA). Electrochemical impedance spectroscopy (EIS) was carried out using a CHI650E electrochemical analyzer (CH Instruments, Austin, TX, USA). X-ray photoelectron spectrometry (XPS, ESCALAB 250Xi, ThermoFisher, Waltham, MA, USA) was applied to the surface compositions analysis of the pristine MoS_2 and Ce/MoS_2 composites. UV-visible diffuse reflectance spectroscopy (DRS) was recorded on a Carry 500-Scan spectrophotometer.

Photocatalytic Activity Measurement

The photocatalytic activity of the composite was evaluated by the reduction of Cr(VI) (mg/L) under a Xe lamp (300 W) equipped with a UV-cut off filter ($\lambda \geq 420$ nm). The impact of thermal catalysis was prevented by using a ventilating fan. All experiments were conducted at room temperature in air. In a typical photocatalytic experiment, 0.03 g of composites were totally dispersed in 100 mL of 50 mg/L Cr(VI) aqueous solution with 20 mmol/L of citric acid. After stirring for 60 min in the dark to ensure absorption-desorption equilibrium, the suspensions were exposed to visible-light irradiation under magnetic stirring. During the illumination reaction process, about 4.0 mL reaction solution was collected at 30 min intervals and then centrifuged to remove the catalyst completely. The remaining amount of Cr(VI) was analyzed using an ultraviolet-visible-light (UV-vis) spectrophotometer (T6 new century, Beijing Puyi General Instrument Co. LTD., Beijing, China), determined at 540 nm. The concentration of total (Cr(III) + Cr(VI)) in aqueous phase was measured using an inductively coupled plasma atomic emission spectroscopy (ICP-OES Optima 3000, Perkin Elmer Inc., Waltham, MA, USA).

RESULTS AND DISCUSSION

Effect of ILs on the Morphology and Properties of MoS_2

To investigate the influence of ILs on the properties of MoS_2 under microwave radiation, the pristine MoS_2 samples were prepared *via* MAIL method using IL(1) through IL(4) as the medium without adding cellulose.

The crystalline phases of the MoS_2 samples prepared in different ILs were studied by XRD characterization. Figure 1 shows the XRD spectra of MoS_2-IL1 through MoS_2-IL4, in which diffraction peaks appearing at $2\theta = 8.76$ °, 17.46 °, 33.50 °, and 58.33 ° are observed in each sample, indexing to (002), (004), (100), and (110) reflections from the layered MoS_2 structure (Liu *et al.* 2015). The intercalation of NH_4^+ ions in layered MoS_2 widens the spacing of the layers, resulting in the shift of (002) diffraction towards lower angles (Bissessur *et al.* 2002). Moreover, the XRD peak intensity of MoS_2-IL1 is obviously higher than those of the others. No impurity peak was found in MoS_2-IL1, which suggests higher crystallinity and higher purity of products prepared in IL(1) by MAIL method.

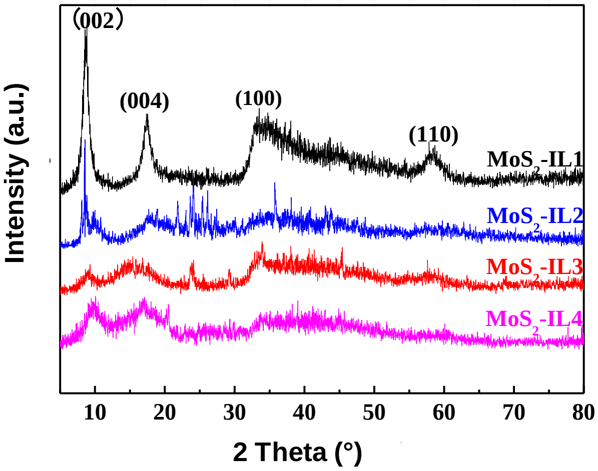

Fig. 1. XRD patterns of MoS_2 prepared in different ionic liquids

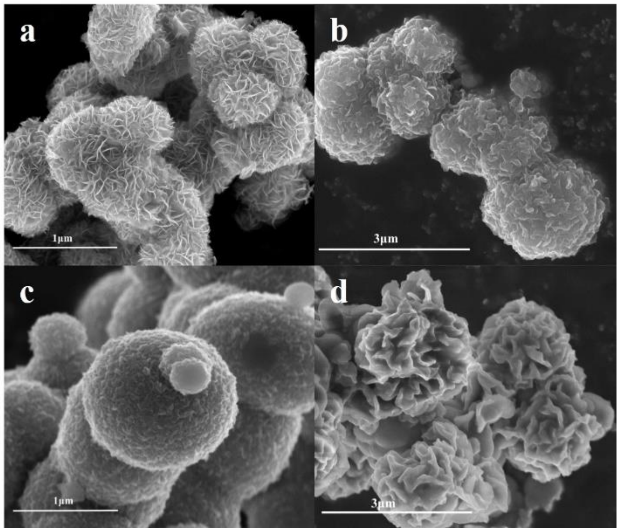

Fig. 2. SEM images of MoS_2-IL1 (a), MoS_2-IL2 (b), MoS_2-IL3 (c) and MoS_2-IL4 (d)

The effects of the ILs on the size and morphology of the MoS_2 samples (MoS_2-IL1 through MoS_2-IL4) were examined by SEM. As shown in Fig. 2a, the SEM image of MoS_2-IL1 displays three-dimensional (3D) metal sulfide flower-like microspheres assembled tightly from many curved two-dimensional (2D) MoS_2 nanoparticles. The MoS_2-IL2 was constructed of rough clusters having irregular surface structure, as illustrated in Fig. 2b. Figure 2c shows the SEM image of MoS_2-IL3, which displays microspheric particles with a mean diameter of 1.5 μm. The MoS_2-IL4 had carnation flower-like structure, and the surface of the sample was constructed of sheet-like structures, as shown in Fig. 2d. The results indicates that the ionic liquid had an important influence on the morphology of MoS_2. Different anions bring about different interactions between IL and ammonium parmolybdate and then cause different morphologies of MoS_2 (Ma *et al.* 2008; Lin *et al.* 2017). Then, TEM characterization was used to further observe the morphology of the MoS_2 (see supporting information Fig. S1 in the Appendix), and the results are corresponding to that of the SEM micrographs.

The charge transfer and recombined processes of MoS_2 samples were evaluated by electrochemical impedance spectroscopy (EIS), and the obtained results were fitted using an equivalent circuit, as shown in Fig. S2. The radius of the semicircle reflects the charge-transfer resistance, R_{ct}, which is an important parameter for characterizing the semiconductor-electrolyte charge-transfer process. Higher values of R_{ct} mean lower rates of charge transfer and recombined process (Cheng *et al.* 2016; Finn and Macdonald 2016). In Fig. S2, MoS_2-IL1 displays a narrower semicircle radius than that of others, which indicates lower R_{ct} of MoS_2 and thus lower recombination of photogenerated carriers when IL(1) is used. The results mean that MoS_2-IL1 will show stronger photocurrent and higher photocatalytic performance (Okafor *et al.* 2011; Farag and Hegazy 2013).

Photocatalytic performance of as-prepared MoS_2 samples was evaluated by the degradation of 20 mg/L RhB solutions under visible light irradiation. The results are presented in Fig. S3. Before visible light irradiation, the mixture of samples and RhB solution were shaken in the dark for 60 min to achieve adsorption-desorption balance. The MoS_2 samples show different adsorption and catalytic behaviors, which could be roughly determined by the slope of the curves. This result demonstrates that MoS_2-IL1 presented higher photocatalytic activity than others. The probable reason might be due to the lower recombination of photogenerated carriers of MoS_2-IL1, and also to the open porous structure of the IL1 form by the 2D nanosheets assembled together (Fig. 2(a)).

Based on the above results, the MoS_2 prepared in IL(1) *via* MAIL exhibited better crystallinity and higher photocatalytic activity. Hence, IL1, which was also excellent for cellulose dissolution, would be used further to prepare Ce/MoS_2 composite materials by MAIL for subsequent experiments. Effects of cellulose support on the structures, morphologies, and photocatalytic properties of the composites will be discussed.

Effect of Temperature on the Morphology of MoS_2 Prepared in IL(1)

Effect of the temperature on the morphology of MoS_2 nanoparticles was also investigated using IL(1) as solvent. As shown in Fig. S4, the MoS_2 samples were present as bulk when the microwave irradiation temperature was 100 °C. The reason might be that low temperature (100 °C) is not sufficient for effective MoS_2 nucleation and crystal growth. With the irradiation temperature was increased (100 to 180 °C), the 2D interweaved nanosheets gradually appeared, finally forming a flower-like architecture assembled from building blocks of 2D nanopetals. However, higher temperature (≥ 180 °C) would lead to easily decomposition of cellulose support.

Preparation and Characterization of Ce/MoS_2 Composite

The successfully synthesized Ce/MoS_2 composite through MAIL method was first demonstrated by XRD characterization, and the spectrum is illustrated in Fig. 3. Compared to the XRD pattern of cellulose, the spectrum of the composite shows the main diffraction peak of MoS_2 phase along with the Ce characteristic peaks, which appeared at $2\theta = 16.3$ °, 22.5 °, and 35.7 °.

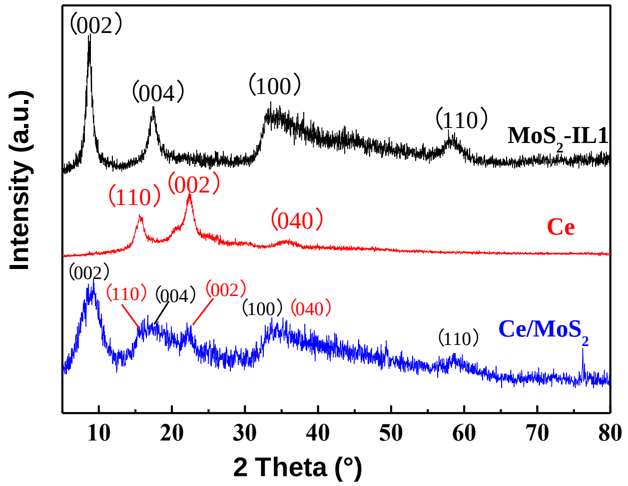

Fig. 3. XRD patterns of cellulose, MoS_2-IL1, and Ce/MoS_2 composite

The general morphology of the Ce after microwave-assisted ionic liquid treatment is shown in Fig. 4a, in which Ce is present as bulk with nothing observed on it. Figures 4b and 4c present the SEM images of Ce/MoS_2 composite, in which many 2D nanoplate-like MoS_2 are tightly anchored on the surface of cellulose, which provide a place for MoS_2 to grow. With the presence of cellulose in the synthetic process, the MoS_2 in the composite presents differently from the pristine MoS_2, which indicates that the growth and assembly process of MoS_2 on the surface of cellulose is hindered. Furthermore, the energy dispersive X-ray spectroscopy (EDS) and corresponding elemental mapping images of the composite

(Fig. 4d) exhibit matched spatial distribution of C, O, Mo, and S, which implies the formation of MoS_2 on the surface of the cellulose.

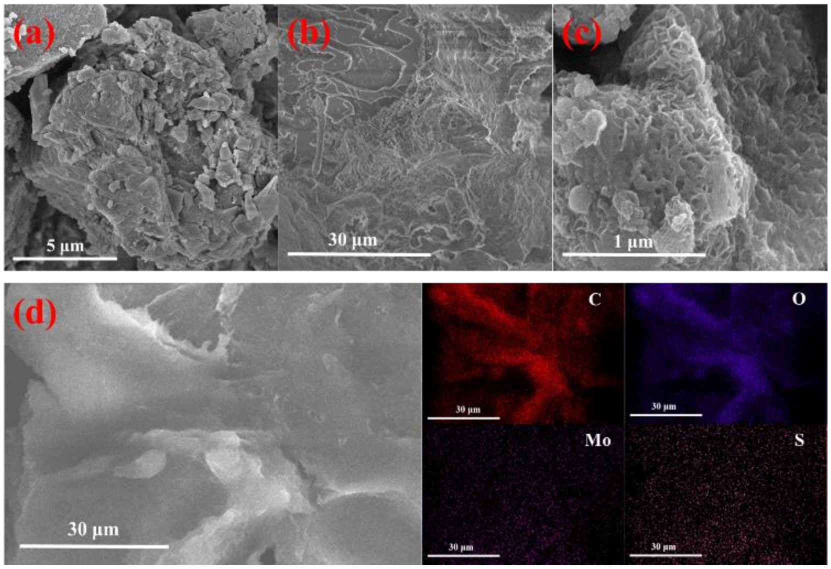

Fig. 4. SEM images of Ce (a), Ce/MoS_2 composite (b, c) and the corresponding elemental mapping images (d)

Additionally, high resolution TEM (HRTEM) observation was performed to further reveal the crystal structure of the MoS_2 with the Ce support (Fig. 5). The lattice spacing of 0.95 nm and 0.56 nm of composite corresponded to the values of (002) and (004) for MoS_2 crystal structure (Zhang *et al.* 2016, 2017).

Similarly, the charge transfer process of Ce/MoS_2 composite materials was measured by EIS, as shown in Fig. S5. Compared with MoS_2-IL1, the narrower radius of Ce/MoS_2 means that the composite is more conductive to the migration of composite carriers, and thus might possess better photocatalytic performance.

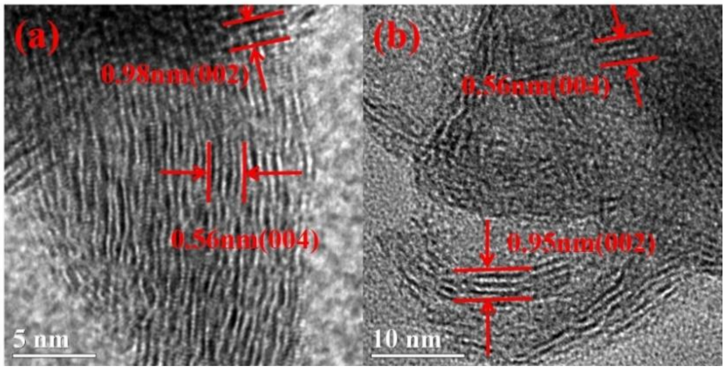

Fig. 5. HRTEM images of pristine MoS_2 (a) and Ce/MoS_2 composite (b)

The surface composition was analyzed by XPS. The results in Fig. S6 demonstrate the appearance of the Mo, S, C, and O elements in the composite. The atomic ratio of Mo/S calculated by the integral area of Mo 3d to S 2p is about 1:1.92, which is close to the stoichiometric ratio of the pristine MoS_2, further confirming the formation of MoS_2 on the Ce surface.

Photocatalytic Reduction of Cr(VI) by Ce/MoS$_2$ Composite

The adsorption-desorption balance plays an important role in determining the starting point for photocatalytic process (Paul *et al.* 2009). The mechanism of the reduction of Cr(VI) to Cr(III) depends on whether Cr(VI) ions are adsorbed on photocatalysts or suspended in solution. Adsorbed Cr(VI) ions might be reduced directly by photoelectrons, while the suspended Cr(VI) ions are reduced indirectly by other species generated from the photocatalysts (Wang *et al.* 2016). The adsorption and photoreduction activity of Ce/MoS$_2$ composite towards Cr(VI) is shown in Fig. 6, in which the pristine MoS$_2$ and Ce are tested as a comparison. A blank test was also conducted to ensure the stability of Cr(VI) in solution under visible light irradiation. The results showed that the as-synthesized nanostructured MoS$_2$ and Ce/MoS$_2$ composite demonstrated strong adsorption capacity towards Cr(VI) under dark conditions, and also excellent photocatalytic reduction activity under visible light irradiation. The support of Ce greatly enhanced the photocatalytic reduction of Cr(VI), from 65.9% to nearly 100% after 180 min illumination.

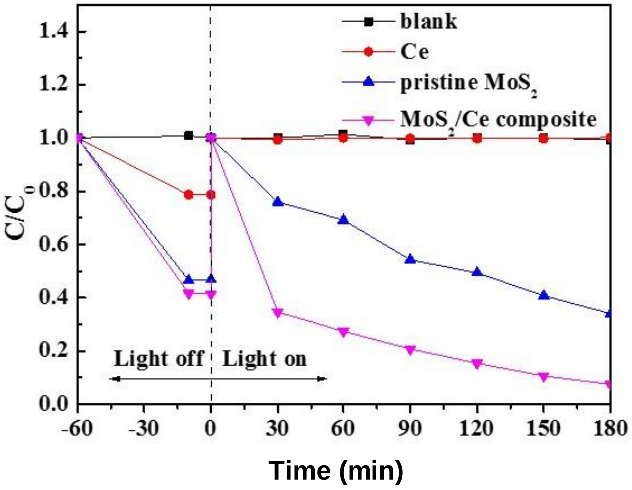

Fig. 6. Photocatalytic reduction of Cr(VI) by Ce, MoS$_2$, and Ce/MoS$_2$ composite under visible-light irradiation. (C_0 = 50 mg/L, dosage = 400 mg/L, pH = 2.0, [CA] = 20 mmol/L)

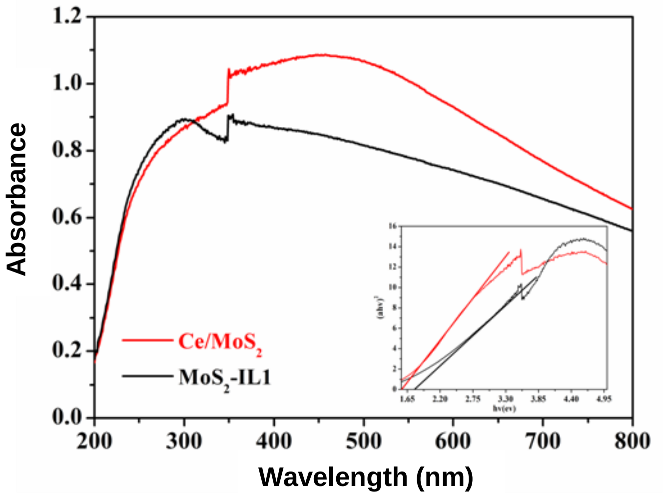

Fig. 7. UV-vis solid absorption spectra and the corresponding band gap values (inset) of MoS$_2$-IL1 and Ce/MoS$_2$ composites

UV-vis DRS was conducted to explain the enhanced photocatalytic activity of Ce/MoS_2 (Fig. 7). In comparison with pristine MoS_2, Ce/MoS_2 composite showed an increased optical absorbance in the visible range. The band gap energy can be estimated from a plot of $(\alpha h\upsilon)^2$ *versus* photon energy ($h\upsilon$) (inset of Fig. 7), which is drawn according to the Tauc plot method (Tauc *et al.* 1966). The intercept of the tangent to the X axis could provide a good approximation of the band gap energy. As shown in inset of Fig. 7, the derived band gaps are estimated to be 1.70 eV and 1.50 eV for MoS_2 and composite, respectively. The narrower band gap energy of composite can be attributed to the chemical bonding between MoS_2 and specific sites of cellulose, and is also the reason for the enhancement of the photocatalytic performance.

The photocatalytic reduction of Cr(VI) to Cr(III) is strongly pH dependent (Ke *et al.* 2017). The effect of pH at the range of 2.0 to 5.0 on the reduction of Cr(VI) is shown in Fig. 8, which illustrates that lower pH was beneficial to the adsorption and photocatalytic reduction of Cr(VI). The high adsorption capacity at low pH might be due to the fact that the positive charged surface caused by the surrounding of abundant H^+ favored the adsorption of the major species Cr(VI) of $Cr_2O_7^{2-}$ and CrO_4^- *via* electrostatic attraction. On the other hand, pH value could influence the redox potential of $Cr_2O_7^{2-}/Cr^{3+}$ from Eq. 1 to Eq. 3, which indicate higher redox potential of $Cr_2O_7^{2-}/Cr^{3+}$ at lower pH value. Therefore, the Ce/MoS_2 composite would show higher photoreduction activity at lower pH, and the subsequent experiment was conducted at pH 2.

$$Cr_2O_7^{2-}+14H^++6e^-\rightarrow 2Cr^{3+}+7H_2O\ E^0=0.98eV \qquad (1)$$

$$Cr_2O_7^{2-}+8H^++3e^-\rightarrow Cr^{3+}+4H_2O\ E^0=0.56eV \qquad (2)$$

$$Cr_2O_7^{2-}+4H_2O+3e^-\rightarrow Cr(OH)_3+5OH^-\ E^0=0.24eV \qquad (3)$$

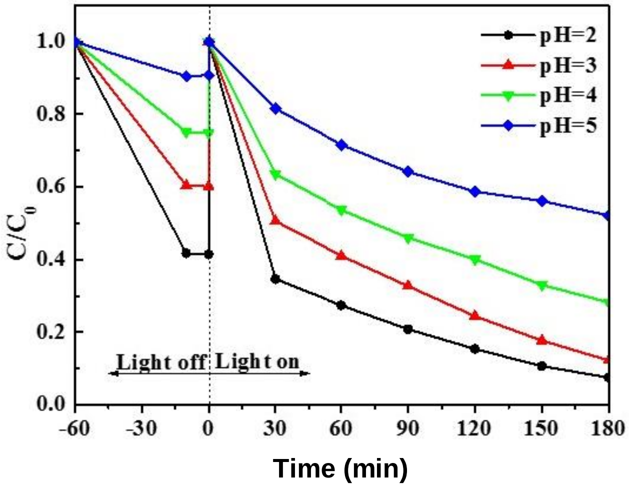

Fig. 8. The effect of the initial pH on photocatalytic reduction of Cr(VI)

When the reduction reaction was carried out in the presence of citric acid (CA), the Cr(VI) reduction rate was greatly enhanced, as shown in Fig. S7. The CA here is thought to have acted as a hole scavenger to dissipate the holes in the photocatalyst (Patnaik *et al.* 2018), thus preventing the effective recombination of the photoelectron and hole, leading to the increase in the photocatalytic reduction of Cr(VI).

Proposed Reduction Mechanism for Cr(VI) by Ce/MoS_2 Composite

To gain insights into the reduction mechanism of Cr(VI) by Ce/MoS_2 composite, XPS was used to analyze the surface composition of the Ce/MoS_2 before and after photocatalytic reduction of Cr(VI).

As presented in Fig. 9, when dark adsorption of Cr(VI) took place, a new peak appeared at around 580 eV, which corresponded to the Cr 2p binding energy (Bissessur *et al.* 2002), indicating the adsorption of Cr on the composite. After visible light irradiation, the spectrum changed unremarkably. The binding energies at around 577 eV to 578 eV from the high-resolution spectra of Cr presented in Fig. 9(b) can be assigned to Cr(III) species (Olsson and Hörnström 1994; Stypula and Stoch 1994), implying the presence of Cr(III) on the surface of Ce/MoS_2 composite. Namely, the reduction of Cr(VI) to Cr(III) happens even in the initial dark adsorption stage. Additionally, the higher intensity of Cr(III) peak after visible-light irradiation signified that more Cr(III) had appeared, which demonstrated the subsequent photocatalytic reduction of remaining Cr(VI) under visible-light irradiation. The XPS results reveal that the reduction of Cr(VI) to Cr(III) is an adsorption-coupled reduction process at first stage and then followed by the photocatalytic reduction process.

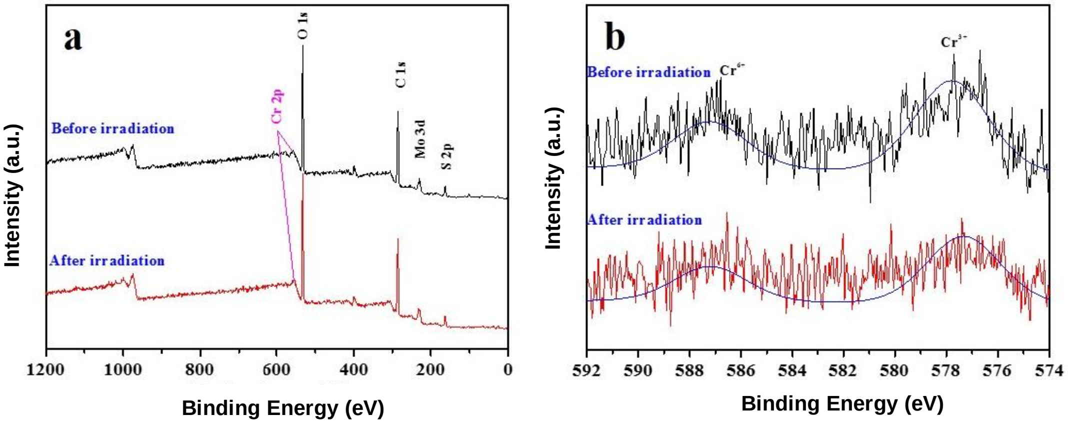

Fig. 9. XPS spectra Ce/MoS_2 composite before and after visible-light irradiation (a); High-resolution spectra of Cr 2p before and after visible-light irradiation (b)

It is assumed that the reduction of Cr(VI) with the photocatalyst can be negligible under dark adsorption, but the results from XPS show that some of Cr(VI) is reduced to Cr(III) partially during the dark adsorption process. To confirm the reduction of Cr(VI) to Cr(III) in the absence of visible-light irradiation, the concentration of total chromium ions and Cr(VI) are measured respectively. As shown in Fig. 10a, the concentration of Cr(VI) decreased during the first dark adsorption, while the total concentration of chromium ions (Cr(VI) + Cr(III)) decreased more steadily. The deviation of the concentration in the first 1 h indicate the formation of Cr(III) ions during the dark adsorption process. After visible light irradiation, the electron-hole pairs are generated on the surface of the photocatalyst and then migrate to the surface of the Cr(VI) particles, which leads to the photoreduction of Cr(VI) to Cr(III) by the photogenerate electrons. The simultaneous reduction of Cr(VI) to Cr(III) during dark adsorption might be thought to be due to the presence of the citric acid, which is considered as highly reductive (Bissessur *et al.* 2002). To confirm the effect of citric acid, the concentration changes of total chromium ions (Cr(VI) + Cr(III)) and Cr(VI) ions in solution without citric acid were measured (Fig. 10b). Figure 10b shows that the Cr(VI) concentration was almost the same with that of total chromium ions (Cr(VI) + Cr(III)) ions during the first dark adsorption process, which illustrates that the spontaneous reduction of Cr(VI) did not occur without visible-light irradiation in the absence of citric acid. Additionally, the reduction rate of Cr(VI) after irradiation was slower compared with that in the presence of citric acid. The citric acid here is considered to act to scavenge the valence band hole and prevent the recombination of electron and hole pairs on the photocatalyst surface, thus accelerating the reduction of Cr(VI).

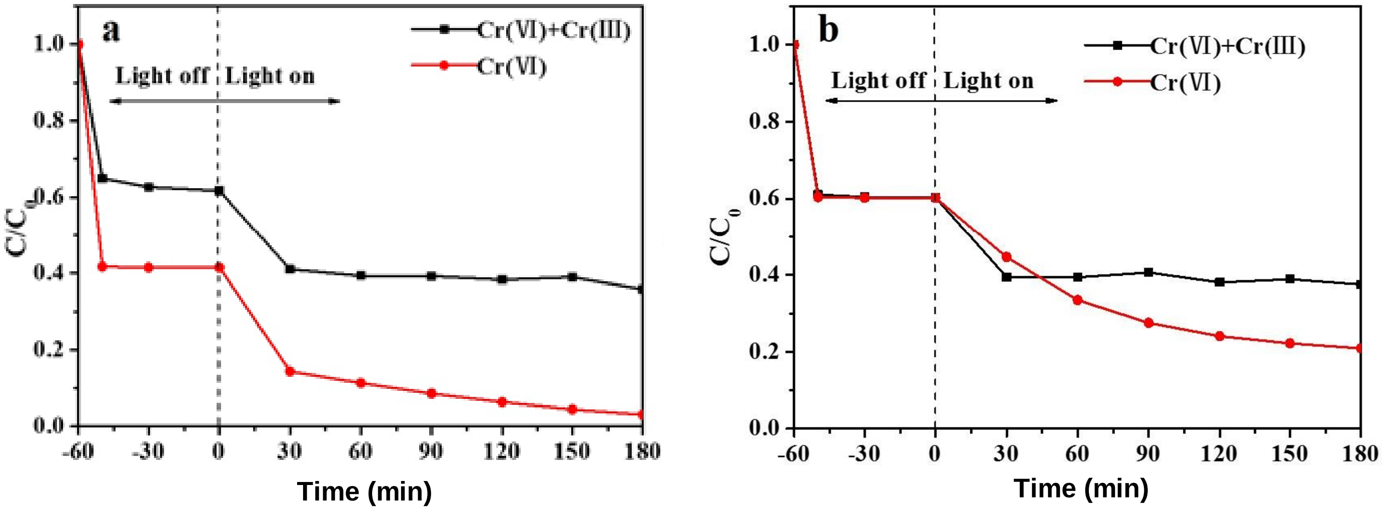

Fig. 10. Concentration of the total Cr ions and Cr(VI) ions in solution (a) with and (b) without citric acid

Stability of the Ce/MoS$_2$ Composite

The stability and reusability of the photocatalyst are crucial for its practical and economical application. The regeneration and reuse tests of Ce/MoS$_2$ composite were carried out, with the result shown in Fig. S8. After three circulating runs, the composite exhibited stable photocatalytic performance with nearly 80% reduction rate of Cr(VI), which indicated strong stability and reusability of the Ce/MoS$_2$ composite.

CONCLUSIONS

1. The Ce/MoS$_2$ composite catalyst was successfully prepared *via* the microwave-assisted ionic-liquid (MAIL) method using cotton as starting materials. The type of ILs used greatly influenced the morphology of MoS$_2$.
2. The as-synthesized IL(1)-mediated Ce/MoS$_2$ composite showed strong adsorption capacity towards Cr(VI) and higher photocatalytic reduction rate of Cr(VI) to Cr(III) in comparison with the pristine MoS$_2$. The enhancement of photocatalytic reduction rate when Ce-supported might be ascribed to the efficient migration of composite carriers.
3. The addition of citric acid as a hole scavenger or to lower pH value of solution would favor the photocatalytic reduction of Cr(VI). Further investigation by the comparison of XPS spectra before and after visible-light irradiation indicated that the simultaneous

reduction of Cr(VI) occurred during the initial dark adsorption process. The reason might be due to the effect of the citric acid as a hole scavenger. Namely, the Cr(VI) removal by Ce/MoS_2 composite was an adsorption-coupled reduction process.

4. The regeneration and reuse test implied that Ce/MoS_2 composite could maintain over 80% Cr(VI) reduction efficiency in the third cycle, which implied the potential use of Ce/MoS_2 composite for the removal of Cr(VI) from wastewater.

ACKNOWLEDGEMENTS

This research was supported by the National Natural Science Foundation of China (No. 21577018) and the Foundation of Science and Technology Project of Fujian Province Educational Department (JAT160059, JZ160416).

REFERENCES CITED

Ai, K., Ruan, C., Shen, M., and Lu, L. (2016). “MoS_2 nanosheets with widened interlayer spacing for high-efficiency removal of mercury in aquatic systems,” *Adv. Funct. Mater.* 26(30), 5542-5549. DOI: 10.1002/adfm.201601338

Bertoni, F. A., Bellú, S. E., González, J. C., and Sala, L. F. (2014). “Reduction of hypervalent chromium in acidic media by alginic acid,” *Carbohydr. Polym.* 114, 1-11. DOI: 10.1016/j.carbpol.2014.07.065

Bissessur, R., Haines, R. I., and Brüning, R. (2002). “Intercalation of tetraazamacrocycles into molybdenum disulfide,” *J. Mater. Chem.* 13(1), 44-49. DOI: 10.1039/b208237n

Bora, L. V., and Mewada, R. K. (2017). “Visible/solar light active photocatalysts for organic effluent treatment: Fundamentals, mechanisms and parametric review,” *Renew. Sust. Energ. Rev.* 76, 1393-1421. DOI: 10.1016/j.rser.2017.01.130

Chebeir, M., and Liu, H. (2016). “Kinetics and mechanisms of Cr(VI) formation *via* the oxidation of Cr(III) solid phases by chlorine in drinking water,” *Environ. Sci. Technol.* 50(2), 701-710. DOI: 10.1021/acs.est.5b05739

Cheng, C.-K., Lin, C.-H., Wu, H.-C., Ma, C.-C. M., Yeh, T.-K., Chou, H.-Y., Tsai, C.-H., and Hsieh, C.-K. (2016). “The two-dimensional nanocomposite of molybdenum disulfide and nitrogen-doped graphene oxide for efficient counter electrode of dye-sensitized solar cells,” *Nanoscale Res. Lett.* 11(1), 117. DOI: 10.1186/s11671-016-1277-0

Christoforidis, K. C., and Fornasiero, P. (2017). “Photocatalytic hydrogen production: A rift into the future energy supply,” *ChemCatChem* 9(9), 1523-1544. DOI: 10.1002/cctc.201601659

Ciesla, P., Kocot, P., Mytych, P., and Stasicka, Z. (2004). “Homogeneous photocatalysis by transition metal complexes in the environment,” *Journal of Molecular Catalysis A Chemical* 224(1), 17-33. DOI: 10.1016/j.molcata.2004.08.043

Du, M., Du, Y., Feng, Y., Yang, K., Lv, X., Jiang, N., and Liu, Y. (2018). “Facile preparation of BiOBr/cellulose composites by *in situ* synthesis and its enhanced photocatalytic activity under visible-light,” *Carbohydr. Polym.* 195, 393-400. DOI: 10.1016/j.carbpol.2018.04.092

Farag, A. A., and Hegazy, M. A. (2013). “Synergistic inhibition effect of potassium iodide and novel Schiff bases on X65 steel corrosion in 0.5 M H_2SO_4," *Corros. Sci.* 74, 168-177. DOI: 10.1016/j.corsci.2013.04.039

Finn, S. T., and Macdonald, J. E. (2016). "Contact and support considerations in the hydrogen evolution reaction activity of petaled MoS_2 electrodes," *ACS Appl. Mater. Inter.* 8(38), 25185-25192. DOI: 10.1021/acsami.6b05101

Ge, H., and Ma, Z. (2015). "Microwave preparation of triethylenetetramine modified graphene oxide/chitosan composite for adsorption of Cr(VI)," *Carbohydr. Polym.* 131, 280-287. DOI: 10.1016/j.carbpol.2015.06.025

Hasin, A. A., Gurman, S. J., Murphy, L. M., Perry, A., Smith, T. J., Gardiner, P. H. E. (2010). "Remediation of chromium(VI) by a methane-oxidizing bacterium," *Environ. Sci. Technol* 44(1), 400-405. DOI: 10.1021/es901723c

Hu, X., Hang, Z., Jian, T., Gao, J., Li, Y., and Cui, H. (2017). "Synthesis of few-layer MoS_2 nanosheets-coated TiO_2 nanosheets on graphite fibers for enhanced photocatalytic properties," *Solar Energy Materials & Solar Cells.* 172, 108-116. DOI: 10.1016/j.solmat.2017.07.027

Jiang, B., Gong, Y., Gao, J., Sun, T., Liu, Y., Oturan, N., and Oturan, M. A. (2018). "The reduction of Cr(VI) to Cr(III) mediated by environmentally relevant carboxylic acids: State-of-the-art and perspectives," *J. Hazard. Mater.* 365, 205-226. DOI: 10.1016/j.jhazmat.2018.10.070

Jonoobi, M., Oladi, R., Davoudpour, Y., Oksman, K., Dufresne, A., Hamzeh, Y., and Davoodi, R. (2015). "Different preparation methods and properties of nanostructured cellulose from various natural resources and residues: A review," *Cellulose* 22(2), 935-969. DOI: 10.1007/s10570-015-0551-0

Kafilzadeh, S. (2016). "Isolation and Identification of chromium (VI)-resistant bacteria from Soltan Abad River sediments (Shiraz-Iran)," *Jundishapur Journal of Health Sciences* 8(1), 2252-021X. DOI: 10.17795/jjhs-33576

Ke, T., Guo, H., Zhang, Y., and Liu, Y. (2017). "Photoreduction of Cr(VI) in water using $BiVO_4$-Fe_3O_4 nano-photocatalyst under visible light irradiation," *Environ. Sci. Pollut. Res.* 24(36), 28239-28247. DOI: 10.1007/s11356-017-0255-0

Lefatshe, K., Muiva, C. M., and Kebaabetswe, L. P. (2017). "Extraction of nanocellulose and *in-situ* casting of ZnO/cellulose nanocomposite with enhanced photocatalytic and antibacterial activity," *Carbohydr. Polym.* 164, 301-308. DOI: 10.1016/j.carbpol.2017.02.020

Li, J., Liu, E., Ma, Y., Hu, X., Wan, J., Sun, L., and Fan, J. (2016). "Synthesis of MoS_2 /g-C_3N_4 nanosheets as 2D heterojunction photocatalysts with enhanced visible light activity," *Appl. Surf. Sci.* 364, 694-702. DOI: 10.1016/j.apsusc.2015.12.236

Li, Y., Deng, X., Tian, J., Liang, Z., and Cui, H. (2018). "Ti_3C_2 MXene-derived Ti_3C_2/TiO_2 nanoflowers for noble-metal-free photocatalytic overall water splitting," *Applied Materials Today* 13, 217-227. DOI: 10.1016/j.apmt.2018.09.004

Lin, C., Zhu, M., Zhang, T., Liu, Y., Lv, Y., Li, X., and Liu, M. (2017). "Cellulose/SnS_2 composite with enhanced visible-light photocatalytic activity prepared by microwave-assisted ionic liquid method," *RSC Adv.* 7(20), 12255-12264. DOI: 10.1039/C7RA00558J

Liu, Q., Li, X., He, Q., Khalil, A., Liu, D., Xiang, T., Wu, X., and Song, L. (2015). "Gram-scale aqueous synthesis of stable few-layered 1T-MoS_2: Applications for visible-light-driven photocatalytic hydrogen evolution," *Small* 11(41), 5556-5564. DOI: 10.1002/smll.201501822

Liu, X., Pan, L., Lv, T., Zhu, G., Sun, Z., and Sun, C. (2011). "Microwave-assisted synthesis of CdS﹣reduced graphene oxide composites for photocatalytic reduction of Cr(VI),” *Chem. Commun.* 47(43), 11984. DOI: 10.1039/C1CC14875C

López-García, M., Lodeiro, P., Barriada, J. L., Herrero, R., and Vicente, M. E. S. D. (2010). “Reduction of Cr (VI) levels in solution using bracken fern biomass: Batch and column studies,” *Chem. Eng. J.* 165(2), 517-523. DOI: 10.1016/j.cej.2010.09.058

Ma, L., Chen, W.-X., Li, H., Zheng, Y.-F., and Xu, Z.-D. (2008). “Ionic liquid-assisted hydrothermal synthesis of MoS_2 microspheres,” *Mater. Lett.* 62(6-7), 797-799. DOI: 10.1016/j.matlet.2007.06.062

Ma, M.-G., Zhu, J.-F., Zhu, Y.-J., and Sun, R.-C. (2014). “The microwave-assisted ionic-liquid method: A promising methodology in nanomaterials,” *Chem. - Asian J.* 9(9), 2378-2391. DOI: 10.1002/asia.201402288

Mitra, P., Banerjee, P., Chakrabarti, S., and Bhattacharjee, S. (2013). “Utilization of solar energy for photoreduction of industrial wastewater containing hexavalent chromium with zinc oxide semiconductor catalyst,” *Desalination & Water Treatment.* 51(28-30), 5451-5459. DOI: 10.1080/19443994.2013.770202

Mohamed, M. A., Salleh, W. N. W., Jaafar, J., Ismail, A. F., Mutalib, M. A., Sani, N. A. A., Asri, S. E. A. M., and Ong, C. S. (2016). “Physicochemical characteristic of regenerated cellulose/N-doped TiO_2 nanocomposite membrane fabricated from recycled newspaper with photocatalytic activity under UV and visible light irradiation,” *Chem. Eng. J.* 284, 202-215. DOI: 10.1016/j.cej.2015.08.128

Nahar, S., Zain, M. F. M., Kadhum, A. A. H., Hasan, H. A., and Hasan, M. R. (2017). “Advances in photocatalytic CO_2 reduction with water: A review,” *Materials* 10(6), 629. DOI: 10.3390/ma10060629

Okafor, P. C., Liu, C. B., Zhu, Y. J., and Zheng, Y. G. (2011). “Corrosion and corrosion inhibition behavior of N80 and P110 carbon steels in CO_2-saturated simulated formation water by rosin amide imidazoline,” *Ind. Eng. Chem. Res.* 50(12), 7273-7281. DOI: 10.1021/ie1024112

Olsson, C.-O. A., and Hörnström, S. E. (1994). “An AES and XPS study of the high alloy austenitic stainless steel 254 SMO® tested in a ferric chloride solution,” *Corros. Sci.* 36(1), 141-151. DOI: 10.1016/0010-938X(94)90115-5

Park, D., Yun, Y S., Lee, H W., and Park, J. M. (2008). “Advanced kinetic model of the Cr(VI) removal by biomaterials at various pHs and temperatures,” *Bioresource Techn.* 99(5), 1141-1147. DOI: 10.1016/j.biortech.2007.02.025

Patnaik, S., Swain, G., and Parida, K. M. (2018). “Highly efficient charge transfer through a double Z-scheme mechanism by a Cu-promoted MoO_3/g-C_3N_4 hybrid nanocomposite with superior electrochemical and photocatalytic performance,” *Nanoscale* 10(13), 5950-5964. DOI: 10.1039/C7NR09049H

Paul, A. K., Madras, G., and Natarajan, S. (2009). “Adsorption-desorption and photocatalytic properties of inorganic-organic hybrid cadmium thiosulfate compounds,” *Phys. Chem. Chem. Phys.* 11(47), 11285-11296. DOI: 10.1039/b913407g

Periyasamy, S., Gopalakannan, V., and Viswanathan, N. (2017). “Fabrication of magnetic particles imprinted cellulose based biocomposites for chromium(VI) removal,” *Carbohydr. Polym.* 174, 352-359. DOI: 10.1016/j.carbpol.2017.06.029

Remoundaki, E., Hatzikioseyian, A., and Tsezos, M. (2010). “A systematic study of chromium solubility in the presence of organic matter: Consequences for the treatment of chromium-containing wastewater,” *J. Chem. Technol. Bio.* 82(9), 802-808. DOI: 10.1002/jctb.1742

Qu, J., Chen, D., Li, N., Xu, Q., Li, H., He, J., and Lu, J. (2017). "Coral-inspired nanoscale design of porous SnS_2 for photocatalytic reduction and removal of aqueous Cr (VI),"*Appl. Catal. B - Environ.* 207, 404-411. DOI: 10.1016/j.apcatb.2017.02.050

Schaumann, J., Loor, M., Ünal, D., Mudring, A., Heimann, S., Hagemann, U., Schulz, S., Maculewicz, F., and Schierning, G. (2017). "Improving the *zT* value of thermoelectrics by nanostructuring: Tuning the nanoparticle morphology of Sb_2Te_3 by using ionic liquids," *Dalton Trans.* 46(3), 656-668. DOI: 10.1039/C6DT04323B

Schütz, M. B., Xiao, L., Lehnen, T., Fischer, T., and Mathur, S. (2017). "Microwave-assisted synthesis of nanocrystalline binary and ternary metal oxides," *Int. Mater. Rev.* 63(6), 341-374. DOI: 10.1080/09506608.2017.1402158

Shindume, H. L., Zhao, Z., Wang, N., Liu, H., Umar, A., Zhang, J., Wu, T., and Guo, Z. (2019). "Enhanced photocatalytic activity of B, N-codoped TiO_2 by a new molten nitrate process," *J. Nanosci. Nanotechno.* (2), 839-849. DOI: 10.1166/jnn.2019.15745

Soto, M., Vajtai, R., Ajayan, P. M., and Barrera, E. V. (2018). "Carbon nanotube conditioning. Part 1 - Effect of interwall interaction on the electronic band gap of double-walled carbon nanotubes," *Nanotechnology.* 29(4), 045701. DOI: 10.1088/1361-6528/aa9f05

Stypula, B., and Stoch, J. (1994). "The characterization of passive films on chromium electrodes by XPS," *Corros. Sci.* 36(12), 2159-2167. DOI: 10.1016/0010-938X(94)90014-0

Sun, B., Qian, Y., Liang, Z., Guo, Y., Xue, Y., Tian, J., and Cui, H. (2019). "Oxygen vacancy-rich BiO_2-x ultra-thin nanosheet for efficient full-spectrum responsive photocatalytic oxygen evolution from water splitting," *Sol. Energ. Mat. Sol. C.* 309-317. DOI: 10.1016/j.solmat.2019.03.030

Szczepanik, B. (2017). "Photocatalytic degradation of organic contaminants over clay-TiO_2 nanocomposites: A review," *Appl. Clay Sci.* 141, 227-239. DOI: 10.1016/j.clay.2017.02.029

Tauc, J., Grigorovici, R., and Vancu, A. (1966). "Optical properties and electronic structure of amorphous germanium," *Physica Status Solidi* 3(1), 37-46. DOI: 10.1002/pssb.1966015022.

Tyrrell, S., Behrendt, G., and Nockemann, P. (2015). "Ionothermal syntheses of nano- and microstructured ternary copper-indium-chalcogenides," *Inorg. Chem.* 54(9), 4495-4503. DOI: 10.1021/acs.inorgchem.5b00322

Wang, C.-C., Du, X.-D., Li, J., Guo, X.-X., Wang, P., and Zhang, J. (2016). "Photocatalytic Cr(VI) reduction in metal-organic frameworks: A mini-review," *Appl. Catal. B* 193, 198-216. DOI: 10.1016/j.apcatb.2016.04.030

Wang, X., Hong, M., Zhang, F., Zhuang, Z., and Yu, Y. (2016). "Recyclable nanoscale zero valent iron doped g-C_3N_4/MoS_2 for efficient photocatalytic of RhB and Cr(VI) driven by visible light," *ACS Sustain. Chem. Eng.* 4(7), 4055-4063. DOI: 10.1021/acssuschemeng.6b01024

Wang, Z., and Mi, B. (2017). "Environmental applications of 2D molybdenum disulfide (MoS_2) nanosheets," *Environ. Sci. Technol.* 51(15), 8229-8244. DOI: 10.1021/acs.est.7b01466

Wang, S., He, F., and Dong, P. (2018). "Simultaneous morphology, band structure, and defect optimization of graphitic carbon nitride microsphere by the precursor concentration to boost photocatalytic activity," *J. Mater. Res.* (23), 3917-3927. DOI: 10.1557/jmr.2018.342

Yang, R.-T., Yu, H.-Y., Song, M.-L., Zhou, Y.-W., and Yao, J.-M. (2016). "Flower-like zinc oxide nanorod clusters grown on spherical cellulose nanocrystals *via* simple chemical precipitation method," *Cellulose* 23(3), 1871-1884. DOI: 10.1007/s10570-016-0907-0

Yin, B. Y. B., and Liu, C. L. C. (2018). "Convenient synthesis and enhanced photocatalytic activity of BiOI/BiOBr nanostructures with different morphologies," *J. Nanosci. Nanotechno.* 18(7), 4771-4779. DOI: 10.1166/jnn.2018.15273

Zhang, Y., Xu, L., Zhao, L., Peng, J., Li, C., Li, J., and Zhai, M. (2012). "Radiation synthesis and Cr(VI) removal of cellulose microsphere adsorbent," *Carbohydr. Polym.* 88(3), 931-938. DOI: 10.1016/j.carbpol.2012.01.040

Zhang, X., Lai, Z., Tan, C., and Zhang, H. (2016). "ChemInform abstract: Solution-processed two-dimensional MoS_2 nanosheets: Preparation, hybridization, and applications," *Cheminform.* 47(38), 8816-8838. DOI: 10.1002/chin.201638201

Zhang, Y., Yin, Z., Dai, C., Zhou, X., and Chen, W. (2016). "Interfacial thermodynamics and kinetics of sorption of diclofenac on prepared high performance flower-like MoS_2," *J Colloid Interface Sci.* 481, 210-219. DOI: 10.1016/j.jcis.2016.07.046

Zhang, D., Jiang, C., Li, P., and Sun, Y. (2017). "Layer-by-layer self-assembly of Co_3O_4 nanorod-decorated MoS_2 nanosheet-based nanocomposite toward high-performance ammonia detection," *ACS Appl. Mater. Inter.* 9(7), 6462-6471. DOI: 10.1021/acsami.6b15669

Zhang, L., Niu, C., Liang, C., Wen, X., Huang, D., Guo, H., Zhao, X., and Zeng, G. (2018). "One-step in situ synthesis of CdS/SnO_2 heterostructure with excellent photocatalytic performance for Cr(VI) reduction and tetracycline degradation," *Chem. Eng. J.* 863-875. DOI: 10.1016/j.cej.2018.07.102

Zhao, Y., Xie, X., Zhang, J., Liu, H., Ahn, H.-J., Sun, K., and Wang, G. (2015). "Frontispiece: MoS_2 nanosheets supported on 3D graphene aerogel as a highly efficient catalyst for hydrogen evolution," *Chem. - Eur. J.* 21(45), 15908-15913. DOI: 10.1002/chem.201584561

Zhou, Z., Peng, X., Zhong, L., Wu, L., Cao, X., and Sun, R. C. (2016). "Electrospun cellulose acetate supported Ag@AgCl composites with facet-dependent photocatalytic properties on degradation of organic dyes under visible-light irradiation," *Carbohydr. Polym.* 136, 322-328. DOI: 10.1016/j.carbpol.2015.09.009

Article submitted: January 27, 2018; Peer review completed: May 13, 2019; Revised version received: May 28, 2019; Accepted: June 2, 2019; Published: June 13, 2019.
DOI: 10.15376/biores.14.3.6114-6133

APPENDIX

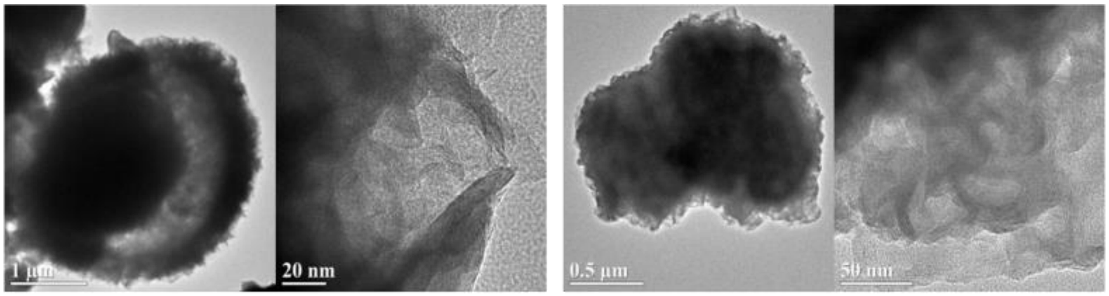

(a) MoS_2-IL1 (b) MoS_2-IL2

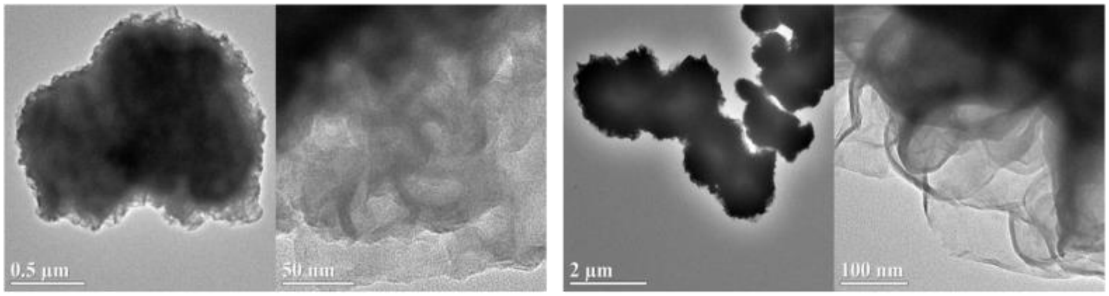

(c) MoS_2-IL3 (d) MoS_2-IL4

Fig. S1. TEM images of MoS_2 prepared in different ionic liquids

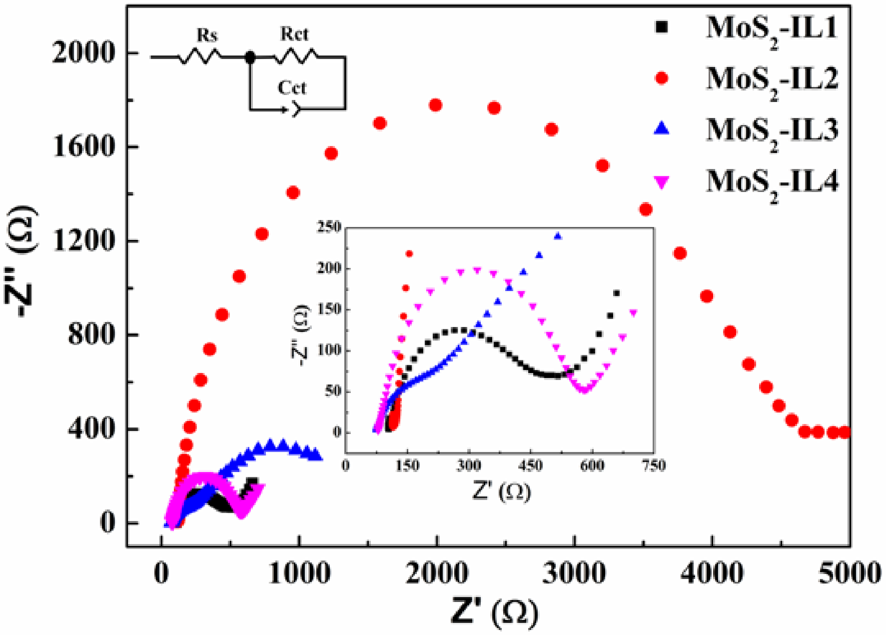

Fig. S2. EIS images of MoS_2 prepared in different ionic liquids

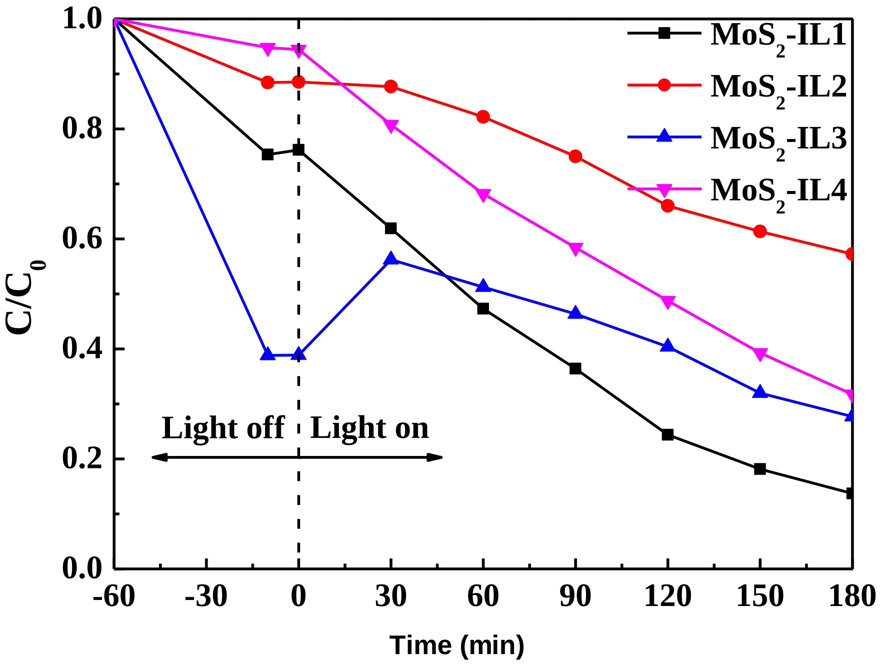

Fig. S3. Photocatalytic performance of as-prepared MoS$_2$ samples by the degradation of 20 mg/L RhB solutions under visible-light irradiation

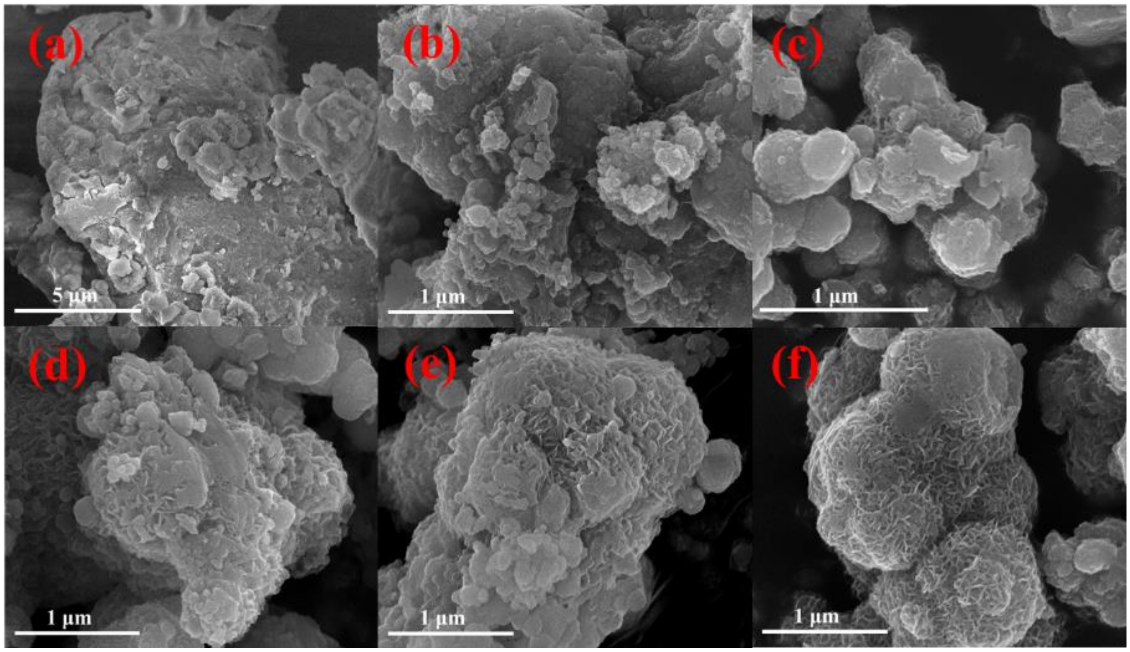

Fig. S4. SEM images of MoS$_2$ at 80 °C (a), 100 °C (b), 120 °C (c), 140 °C (d), 160 °C (e) and 180 °C (f)

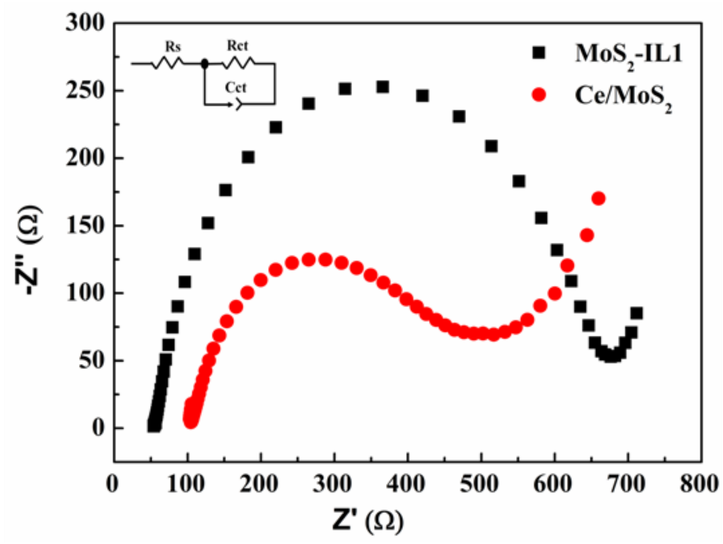

Fig. S5. EIS of MoS$_2$-IL1 and Ce/MoS$_2$ composite

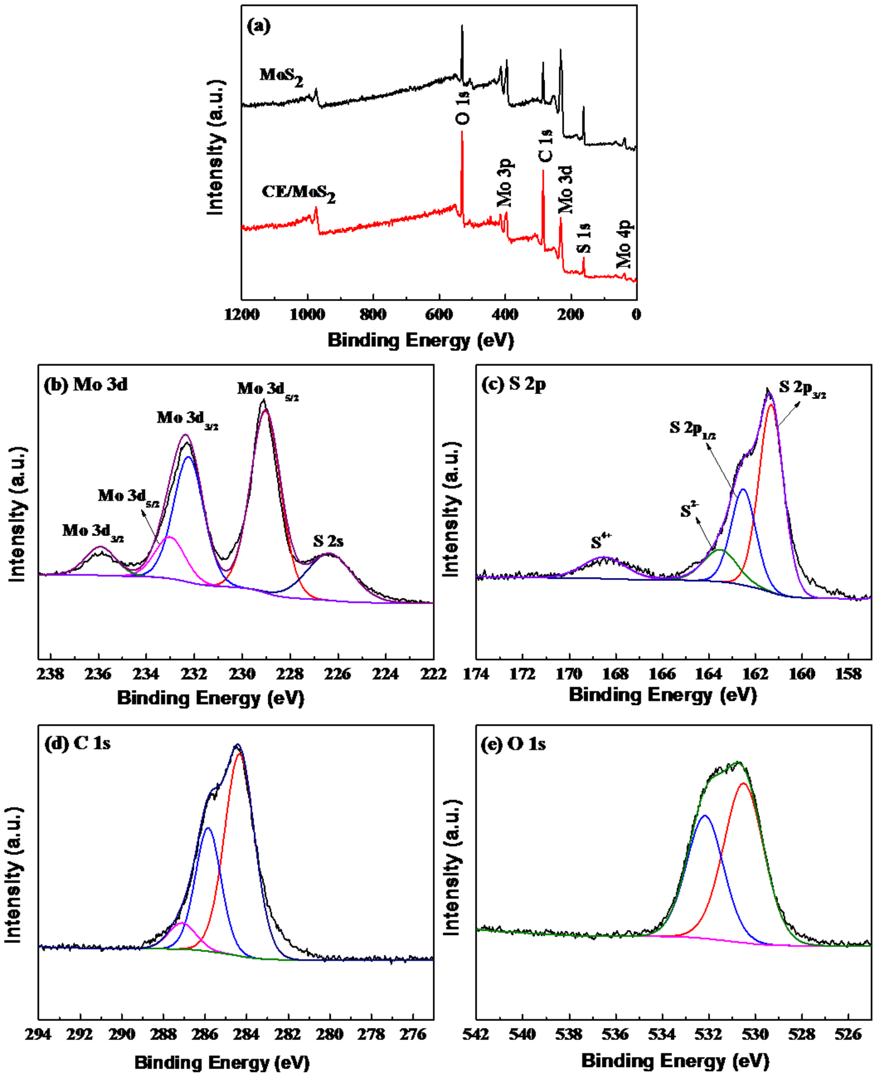

Fig. S6. XPS spectra of pristine MoS$_2$ and Ce/MoS$_2$ composite: (a) survey spectra, (b) Mo 3d, (c) S 2p, (d) C 1s, (e) O 1s

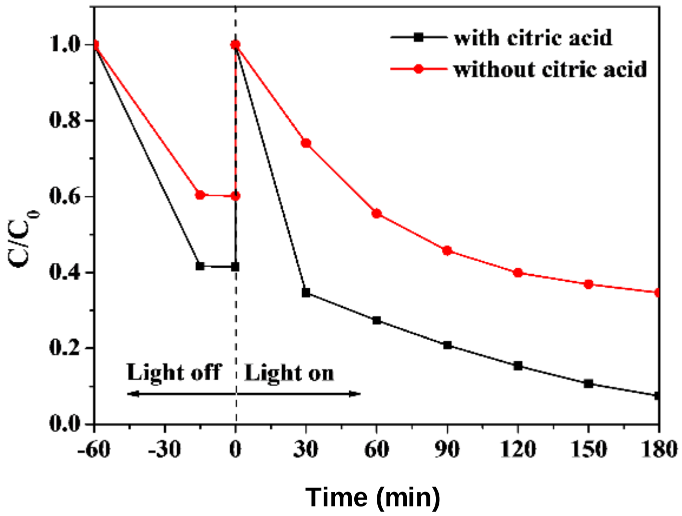

Fig. S7. Effect of the citric acid on photocatalytic reduction of Cr(VI)

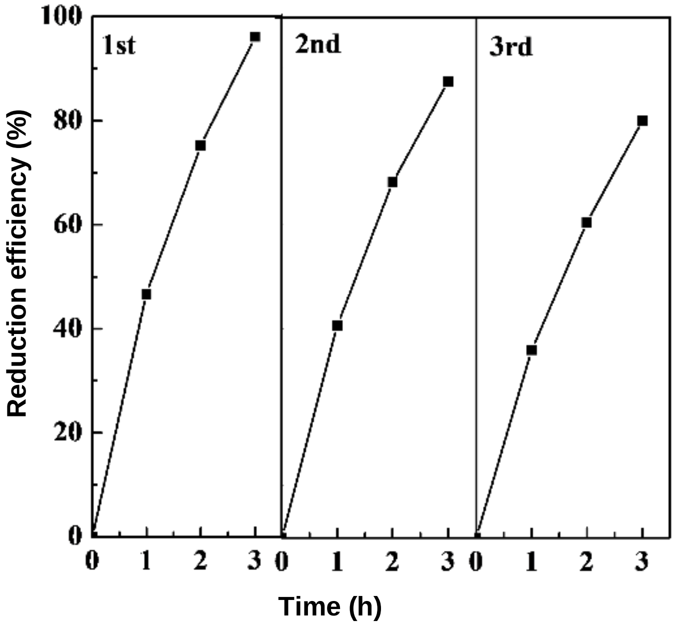

Fig. S8. Effect of recycling times on the photocatalytic reduction of Cr(VI)